Cell Reports
Physical Science

Article

Structural dynamics of a nickel electrocatalyst during water splitting observed via the *operando* pair distribution function

Graphical abstract

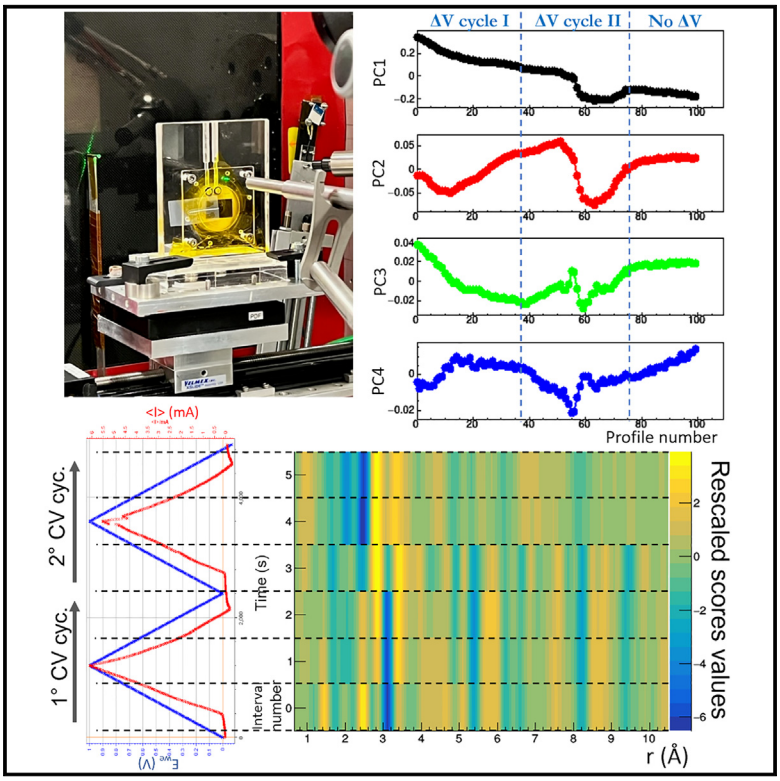

Authors

Rocco Caliandro, Enrico Berretti, Maria V. Pagliaro, ..., Cinzia Giannini, Alessandro Lavacchi, Mario Pagliaro

Correspondence

cinzia.giannini@cnr.it (C.G.), alessandro.lavacchi@cnr.it (A.L.), mario.pagliaro@cnr.it (M.P.)

In brief

Caliandro and Berretti use an *operando* investigation technique relying on synchrotron X-ray powder diffraction merging the pair distribution function, principal-component analysis, and *operando* electrochemistry to investigate an electrocatalyst. NiGraf, composed of nickel-based nanoparticles encapsulating graphene oxide, is monitored throughout the oxygen evolution reaction for insights.

Highlights

- We study the NiGraf electrocatalyst using a new *operando* characterization technique
- NiGraf consists of nickel-based nanoparticles encapsulating graphene oxide
- NiGraf is studied during the oxygen evolution reaction using synchrotron XRPD and PDF
- Analysis unveils key structural changes, including an irreversible activation stage

Caliandro et al., 2024, Cell Reports Physical Science *5*, 102341
December 18, 2024
https://doi.org/10.1016/j.xcrp.2024.102341

CellPress

Cell Reports
Physical Science

CellPress
OPEN ACCESS

Article

Structural dynamics of a nickel electrocatalyst during water splitting observed via the *operando* pair distribution function

Rocco Caliandro,[1,4] Enrico Berretti,[2,4] Maria V. Pagliaro,[2] Rosaria Ciriminna,[3] Vincenzo Mangini,[1] Cinzia Giannini,[1,*] Alessandro Lavacchi,[2,*] and Mario Pagliaro[3,5,*]

[1]Istituto di Cristallografia, CNR, via G. Amendola 122/o, 70126 Bari, Italy
[2]Istituto di Chimica dei Composti Organometallici, CNR, via Madonna del Piano 10, 50019 Sesto Fiorentino, Italy
[3]Istituto per lo Studio dei Materiali Nanostrutturati, CNR, via U. La Malfa 153, 90146 Palermo, Italy
[4]These authors contributed equally
[5]Lead contact
*Correspondence: cinzia.giannini@cnr.it (C.G.), alessandro.lavacchi@cnr.it (A.L.), mario.pagliaro@cnr.it (M.P.)
https://doi.org/10.1016/j.xcrp.2024.102341

SUMMARY

Alkaline water electrolysis based on durable electrocatalysts made from Earth-abundant metals like nickel is a crucial energy storage technology for the transition to renewable energy. Enabling the observation of active catalytic species under working conditions by monitoring the surface oxidation state and local atomic structure transformation, *operando* characterization techniques can probe the active sites and promote a fundamental understanding of the reaction mechanisms. We introduce a technique merging the pair distribution function (PDF), principal-component analysis, and *operando* electrochemistry to investigate the electrocatalyst NiGraf, which is composed of graphene oxide entrapped in nickel-based nanoparticles, during the oxygen evolution reaction. The *operando* investigation of the electrocatalyst uses synchrotron X-ray powder diffraction and PDF. Structural changes in the crystal phases of the nanomaterial during voltammetry cycles in the oxygen evolution reaction range revealed first a reversible variation in the distance between graphene oxide planes and a subsequent irreversible activation stage of the electrocatalyst.

INTRODUCTION

In situ and *operando* techniques are increasingly being applied to study heterogeneous catalysts under operative conditions.[1,2] Particularly, advancements in high-brilliance and high-energy synchrotron X-ray sources, along with faster and more efficient detectors, offer opportunities to conduct *in situ*/*operando* scattering experiments to investigate dynamic properties and time-dependent reaction processes. In the last few years, the pair distribution function (PDF) has been used extensively to study and optimize the design of more efficient batteries.[3,4] In general, PDF measurements provide structural information across different length scales, from the local atomic environment to the long-range structure, allowing the identification of contributions from different crystal phases. Unlike conventional diffraction methods, the PDF does not require long-range order, making it ideal for the study of materials comprising disordered phases, including defect-rich small nanoparticles or amorphous phases. Various electrochemical cells for *in situ*/*operando* electrochemical/X-ray experiments, aimed at minimizing background X-ray scattering from the electrochemical solution and cell walls intersected by the X-ray beam, have been developed in order to study battery materials,[5–7] but very few studies regarding combined *operando* X-ray diffraction (XRD)/electrochemistry on electrocatalysts are presented in the literature and even less on operando PDF.[8] Battery material studies require very low electrolyte volumes; in fact, no change in electrolyte occurs throughout the working life of these devices. This factor permits the use of simplified cell designs, which are easier to implement to minimize the unwanted scattering. On the contrary, electrochemical cells for studies involving electrocatalysts for fuel cells or electrolyzer applications usually need larger amounts of accessible electrolyte at the working electrode (WE), eventually a flux of it, which complicates the cell design for PDF applications. Moreover, we usually have to deal with smaller, disordered electrocatalytic particles with low signal-to-background ratios, limited control over experimental conditions during the electrochemical reaction, and the formation of gas bubbles at the electrodes and predominance of bulk over surface X-ray scattering.

In this context, nickel (alone or alloyed with iron in stainless steel) is the catalyst employed at both the cathode and anode of commercial alkaline water electrolyzers[9] for the electrochemical hydrogen evolution reaction (HER)[10,11] and oxygen evolution reaction (OER).[12,13] Its relatively high activity and far lower cost with respect to rare platinum group metals (PGMs) make it the electrocatalyst of choice for the wider diffusion of alkaline water electrolysis (AWE).[14,15] AWE is already used to manufacture around 1% of the global annual output of hydrogen. Using

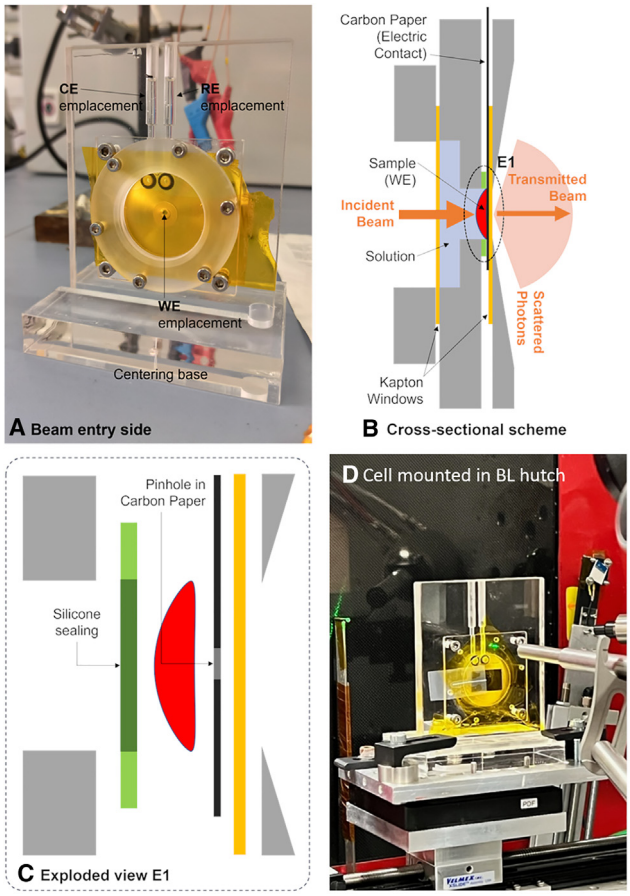

Figure 1. Electrochemical cell developed for *operando* PDF experiments

(A–C) Front (A) and side cross-sectional (B) views of the (C) exploded view (E1) of the working electrode WE setup.

(D) The electrochemical cell mounted at the beamline ID-28-2 at BNL.

electricity from renewable energy sources, the technology will be widely deployed to produce solar (or "green") hydrogen for electric mobility and other end-energy use.[16]

Nickel (II) species like oxides and hydroxides play a pivotal role during OERs in the alkaline environment. Metallic Ni turns into NiO during anodic polarization, which then transforms into α-Ni(OH)$_2$ (disordered phase) and β-Ni(OH)$_2$ (hexagonal, ordered phase) and subsequently to the relative oxyhydroxides, γ-NiOOH (with a formal Ni oxidation state of 3.7) and β-NiOOH (with a formal Ni oxidation state of 3), respectively.[17] Experimental results showed that these oxyhydroxide species, especially the most disordered ones, are responsible for the oxygen evolution catalytic activity of this material.[17] Their ratio in Ni-based materials, and the reversibility between Ni^{2+} and Ni^{3+} species, is strongly dependent on the electrocatalyst synthesis method.[18] In recent years, plentiful research efforts have been devoted to increasing the activity of nickel by coupling it with other elements and compounds.[9,19] Among these, graphene oxide (GO) has attracted particular interest due to its conductivity, high surface area, and high chemical and mechanical stability.[20,21] Moreover, also GO acts as an oxidation catalyst,[22] facilitating Ni^{3+} formation, which in turn is active toward the OER[23,24] through the formation of NiOOH species. In all these attempts, however, GO is used as a support that is "decorated" with Ni-based catalytic species. A complementary approach was recently adopted with the introduction of NiGraf, a new molecularly doped metal comprised of three-dimensional (3D) GO entrapped in nickel-based jamborite (Ni(OH)$_2$(NiOOH)) nanoparticles.[25] The catalyst is reproducibly synthesized by a simple one-pot procedure carried out in water starting from a Ni precursor salt, GO, and sodium borohydride as the reducing agent. Three different GO loadings were tested: 0.2%, 1%, and 5% (NG 1, NG 2, and NG 3, respectively). The static PDF characterization of samples at various GO loads allowed the identification of the crystal phases and their structural characterizations, whereas electrochemical studies showed superior electrochemical performances for the OER of samples with added GO.[25] It was observed that the addition of GO induces an order-disorder transition, resulting in a reduction of crystallinity of the jamborite.

Still, several questions remain unanswered: how do the electrochemical properties of the GO@Ni catalysts correlate with their structural features and how do the two crystal phases interact during the electrochemical process, potentially leading to correlated structural changes?

To address these inquiries, we have designed and developed an electrochemical cell for *operando* PDF studies and conducted dedicated synchrotron experiments on NiGraf. The EC cell was designed starting from a previous design of an X-ray absorption spectroscopy (XAS) *operando* cell, modified in order to achieve a simple design, fast and precise sample change, minimal water scattering, and minimization of gas bubbles along the beam path. A substantial amount of collected data was processed using principal-component analysis (PCA) to reduce dimensionality and extract trends in data. PCA was applied to both X-ray powder diffraction (XRPD) and PDF profiles, and the results were interpreted within modulation enhanced diffraction (MED), a theoretical framework that has been developed to interpret the XRD signal from systems subjected to external stimuli.[26,27]

RESULTS

Development of the electrochemical cell for *operando* PDF measurements

The design of the electrochemical cell is derived from a cell previously adopted for XAS experiments[28–30] and modified to fit the typical geometry of synchrotron XRD experiments[3] (Figure S1). The experiment design criteria were focused on decreasing the background scattering from both the liquid electrolyte and the cell materials. For these reasons, the volume of water solution crossed by the X-ray beam was minimized, moving the WE and reference electrode (RE) away from the beamline. In addition, Kapton windows were used due to their high resistance to radiation, relatively low absorption, and very low angle diffraction peaks. PDF measurements necessitate the collection of photons at wide scattering angles in order to enhance the momentum transfer integration. To fulfill this requirement, the position of the sample was shifted from upstream (Figure S1B) to downstream (Figures 1A and 1B) with respect to the beam

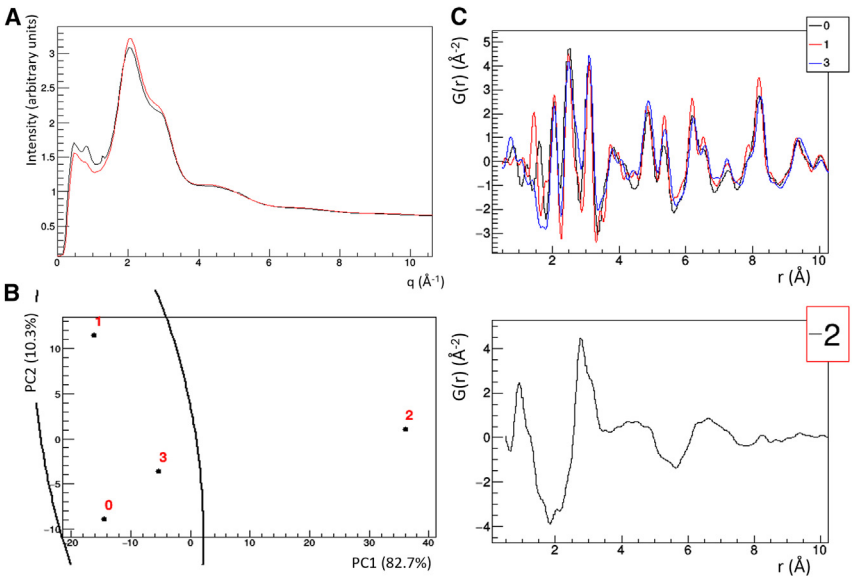

Figure 2. Effect of background on XRPD and PDF profiles

(A) XRPD profiles measured in two different positions (black curve for carbon paper and red curve for pinhole) of the electrochemical cell without a sample.

(B) Score plot of the first two principal components (PC1 and PC2) as obtained by PCA applied to PDF profiles calculated from static measurements with (1) and without (0) background subtraction and from *operando* measurements with (3) and without (2) background subtraction. Each point in this space represents a PDF profile. The fraction of total data variance explained by the PCs is reported in parentheses along the axes. The ellipse shows the result of a hierarchical clustering procedure applied on the points in the score plot.

(C) PDF profiles grouped according to the clustering results.

and the rear wall flared to avoid interference with photons scattered at wide angles (Figures 1B and 1C). This redesigned cell utilizes plexiglass (polymethyl methacrylate [PMMA]) as bulk material. The housing for the sample and the electrolyte solution is accessible via a lid closed with screws, which prevents liquid leakage. Two grooves to hold the counter electrode (CE) and RE were positioned in the upper part. The base substrate for the WE was made by a thin (200 μm) carbon paper (CP) sheet, which was squeezed between the intermediate cell element and the flared support (Figure 1C) in order to prevent solution leakage. A 1 mm pinhole was punched into the CP, to be placed in the center of the hole on the flared cell element. The purpose of the pinhole was dual: (1) to enable electrical contact between the WE and electrocatalyst ink, drop casted on the CP substrate, and (2) to decrease the background signal during the X-ray experiment by targeting the center of the pinhole with the beam. This solution itself represents a novelty in this kind of experiment, where a beam path made as free as possible is mandatory to minimize scattering from unwanted cell elements while still maintaining a sufficient electrical contact with the electrocatalyst for electrochemical cycling. To facilitate sample replacement during measurements, a practical solution was devised: the centering base, fixed to the worktable in the beamline as shown in Figure 1D, is kept separate from the electrolytic cell. The latter can be easily assembled and disassembled from the base by inserting it into a groove on the base, enabling fast positioning of the cell body without further alignment.

The proposed electrochemical cell design permits fast and reproducible assembly of the WE (electrocatalyst) directly in the cell body. Moreover, the cell could be easily implemented as a flux cell by adding an inlet and an outlet to the main chamber, adopting the same criteria used for RE and CE emplacements. This implementation, due to the flux of the electrolyte at the WE, could, in principle, help to get rid of the gases that could form during electrochemical operations.

Calibration of the electrochemical cell

Empty cell measurements were conducted to refine the cell design and establish a reference for background subtraction. Figure 2A illustrates the XRPD profiles collected at two different positions of the cell in a plane perpendicular to the primary X-ray beam, relative to the center of the pinhole (Figure 2A, red) and the CP (Figure 2A, black). Notably, peaks at q = 0.8 and 1.3 $Å^{-1}$ were consequently attributed to the presence of the CP on the beam path. To minimize this effect, we fixed the position of the cell base at the beginning of the experiment and signed the exact position of the mobile part of the cell to retain the same position of the hole with respect to the beam when changing the catalytic samples.

The next step was to acquire the PDF measurements of the complete electrochemical cell under open-circuit potential (OCP) by using the sample with higher crystallinity (NG1) as the target. To assess the impact of the *operando* configuration on the PDF profile calculation, we compared the *in situ* and *ex situ* OCP results, the latter acquired using a glass capillary as the sample holder. For the elaboration of both measurements, a background subtraction was performed (the subtraction of the empty capillary for the *ex situ* measurement). A PCA comparison of the PDF profiles, generated with and without background subtraction (Figure 2B), reveals significant differences between the profiles obtained in *ex situ* and *in situ* OCP conditions. Background subtraction has a minor effect on *ex situ* data, with representative points 0 and 1 spread along PC2, which accounts for only 10.3% of the total data variance. In contrast, background subtraction applied to the *in situ* OCP measurements produces a notable effect, with representative points 2 and 3 separated along PC1, which accounts for 82.7% of the total data variance. Consequently, the background-subtracted *in situ* PDF profile (3) closely resembles those calculated in static conditions (0 and 1), while the *in situ* profile without background subtraction is located outside this cluster. It can be noted that background subtraction changes the *G(r)* profile, making it sharper. Its effect on *in situ* profiles is clearly evident along all values of interatomic distances,

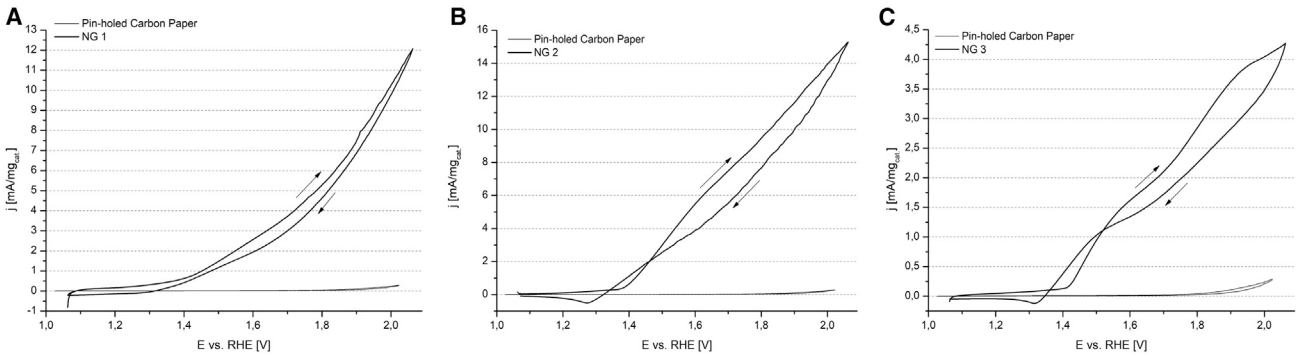

Figure 3. Voltammetry measurements

Voltage applied and current measured in the cyclic voltammetry experiment carried out on NiGraf samples NG1 (A), NG2 (B), and NG2 (C).

while on *ex situ* profiles, it is mainly due to a shift of the first peak from 1.6 to 1.4 Å. The significant effect of background subtraction in *in situ* OCP measurements (Figure 2C) is attributed to the considerably higher scattering power of materials encountered by the X-ray beam passing through the cell (electrolytic solution, Kapton windows, CP) compared to the empty glass capillary.

A closer examination of PDF generation in static and *in situ* setups is presented in Figure S2, which shows the measured XRPD profiles overlaid on the background, the reduced total scattering structure function $F(q)$, and the PDF function $G(r) = \frac{2}{\pi}\int_{q_{min}}^{q_{max}} F(q)\sin(qr)dq$. Despite the markedly different shapes of the profiles measured under static and *in situ* conditions, the corresponding $F(q)$ profiles, calculated after background subtraction, exhibit remarkable similarity. The primary difference lies in the extent of the useful q range: the static $F(q)$ profile retains significant values up to q = 23 Å^{-1}, whereas the *in situ* profile is limited to $q < 17$ Å^{-1} due to fluctuations occurring at higher momentum-transfer values. Despite these differences, the resulting PDF profiles are quite similar, as previously indicated in Figure 2. The parameters used for PDF generation are listed in Table S1.

Operando analysis of sample NG1

Voltage was applied at a 50 mV/min rate between 1 and 2 V vs. reversible hydrogen electrode (RHE). Thus, a full voltammetry cycle took about 40 min. The voltammetric curve for the first cycle is reported in Figure 3A. Throughout the voltammetry experiment, XRPD profiles were continuously acquired, with a total of 39 measurements within a voltammetry cycle.

The data matrix, comprised of the 39 measurements, underwent PCA processing to detect trends with high sensitivity. This fast processing was also employed during the experiment's execution to monitor system responses and make decisions regarding further measurements. Despite seemingly unchanged profiles from one measurement to another (Figure S3A), PCA decomposition revealed well-defined monotonic trends in PC1, explaining 74.7% of the total data variance. This trend was accompanied by a quadratic trend in PC2, explaining 17.2% of the total data variance (Figure S3B). Additionally, PC4, explaining only 2.1% of the total data variance, exhibited a trend strongly correlated to the applied voltage. The loading plot (Figure S3D) can, in principle, be interpreted as the XRPD profile associated with each PC trend. However, due to the nanometric size of the NG1 crystallites resulting in broad XRPD peaks, the experimental setup optimized for PDF measurements reducing the angular resolution of XRPD profiles, and the large contribution of background at low q values, where the most intense components of the scattering signal are found, the information contained within the XRPD profiles (and consequently the loading plots) is of limited utility. To overcome this drawback, we pursued two approaches.

(1) To enhance peak separation peaks, we conducted the *operando* measurement again using a setup optimized for XRPD measurements, with the detector placed further away from the sample. However, under these conditions, the results of the PCA, as depicted in Figure S4, revealed higher fluctuations in the score values. This suggests the presence of random differences among sequentially collected measurements, likely attributable to the extended path (1,411 mm) traveled by scattering photons before reaching the detector. This extended path severely impedes the detection of trends in data across the *operando* measurements.

(2) To enhance interpretability of the PCA loadings, we processed the PDF profiles instead of the XRPD ones. This approach focused on the potential for loading values to contain information about the local structure of the material. However, a notable disadvantage of this approach is that the input for PCA is derived from processing steps (such as the calculation of the normalized total scattering function and sine Fourier transformation[31]) rather than directly measured data.

The results shown in Figures S5 and S6 indicate a significant signal only for PC1. Notably, the shapes of the loadings corresponding to the subsequent component lack physical meaning: their characteristic periodicity in r space is close to $2\pi/Q_{max}$, which corresponds to the expected value for ripple artifacts arising from the finite Q-range.[32] Additionally, their envelope does not exhibit a decreasing trend, typical for a PDF.[32] This observation remains valid whether the background is subtracted from the signal (Figure S6) or not (Figure S5).

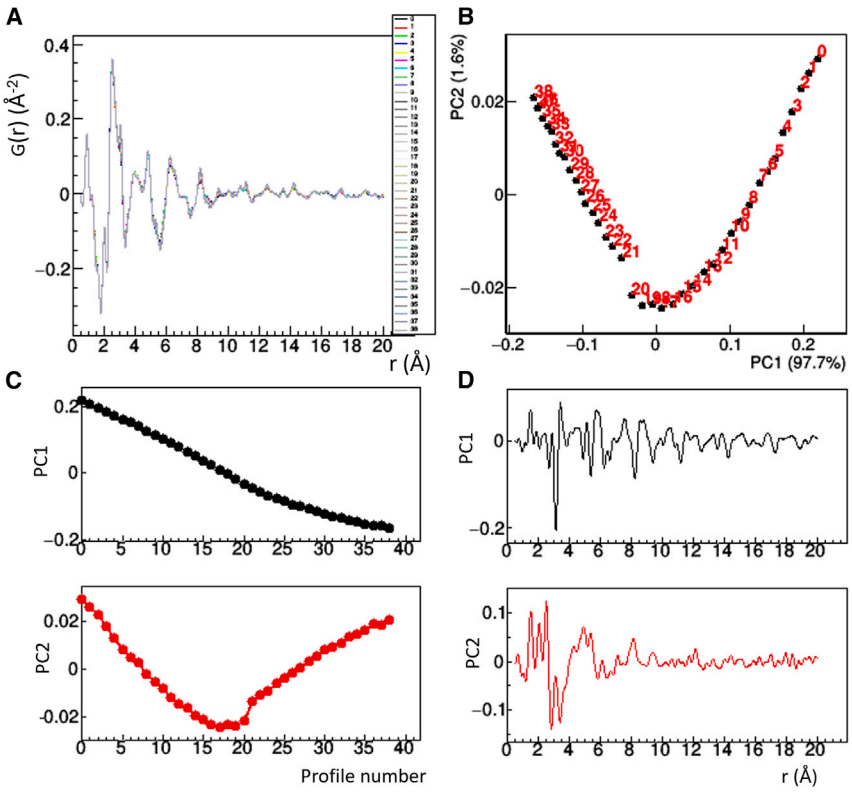

Figure 4. PCA comparison among PDF profiles without background subtraction obtained from *operando* measurements on NiGraf sample NG2

(A) PDF profiles superposed.

(B) Score plot of the first two principal components. The percentage of data variance explained by each component is reported on its axis.

(C) Scores of the first 2 principal components.

(D) Loadings of the first 2 principal components.

Operando analysis of NiGraf sample NG2

The results of the first cycle of the voltammetry/PDF experiment conducted on NiGraf sample NG2 are displayed in Figure 3B. The PCA comparison of the measured XRPD profiles shows a distinct quadratic relationship between the second component, explaining 2.6% of the total data variance, and the first component, explaining 96.6% of the total data variance (Figure S7B). Similar to sample NG1, PC1 scores shows a monotonic trend, but the corresponding loadings appear inverted. It should be noted that both the scores and loadings carry on a sign ambiguity, and only the product (scores × loadings) has a definite sign. Hence, the parabola shown in Figure S7B has a concavity pointing downwards, whereas it points upwards in Figure S3B. Similarly to NG1, XRPD measurements collected in the optimized XRPD setup do not yield significant results (data not shown). However, the PCA applied to PDF profiles proves to be more informative than in the NG1 case (Figure 4). Here, a clear quadratic relationship between PC1 and PC2 scores can be seen in Figure 4B, and the trends in score values depicted in Figure 4C mirror those in the XRPD case (Figure S7C), albeit with opposite signs. Higher PCs are deemed insignificant, according to the criteria mentioned previously.

Despite the significant modification of the PDF profile resulting from background subtraction (Figure 4A vs. Figure S8A), it has a minor effect on the PCA results. Specifically, the score values associated with the first two PCs (Figures 4B and 4C vs. Figure S8B) are very similar, while the loading values exhibit similarity only for PC1 but are rather different for PC2, which explains only a few percent of the total data variance (Figure 4D vs. Figure S8D). This discrepancy arises because background subtraction is consistently applied to all the PDF profiles, resulting in only small-scale variations from one profile to another. However, PCA emphasizes differences among profiles, thus neglecting constant terms introduced by background subtraction.

Operando analysis of NiGraf sample NG3

The outcomes of the first voltammetry/PDF experiment conducted on NiGraf sample NG3 are reported in Figure 3C. The PCA comparison of XRPD profiles is shown in Figure S9. Notably, a quadratic trend of PC2 scores with respect to PC1 scores is still observed, although deviations from this trend are observed for the last measurements of the first voltammetry cycle.

The PCA applied to PDF profiles yields similar trends in scores to those obtained for XRPD profiles only when the background is not subtracted (Figure 5). Instead, background-subtracted PDF profiles decomposed by PCA do not exhibit the expected quadratic relationship between PC1 and PC2 scores as predicted by the MED theory (Figure S10). Since PCA is a blind decomposition driven by the direction of maximum variability in the data, such discrepancies can arise. In order to address this issue, a constrained decomposition method called optimal constrained component rotation (OCCR) can be employed.[33,34] In OCCR, the two PCs determined by PCA, which are necessarily orthogonal to each other, are independently rotated within a global optimization search. This search uses a cost function that rewards solutions for which Equation 1 is fulfilled. Specifically, the cost function is defined as the Pearson correlation coefficient between the second (rotated) score and the square of the first (rotated) score.[33] The best rotation values found were $\phi = -0.970$ rad and $\psi = -0.097$ rad, with an increase of the cost function from 0.49 to 0.97. The scores and loadings obtained by OCCR applied to background-subtracted PDF profiles are shown in Figure S11. It can be noted that the score plot in Figure S11B now shows an approximate quadratic trend, with a parabola having a horizontal axis. It is rotated with respect to that of the parabola shown in Figure S10B as a result of the rotation of the first two PCs.

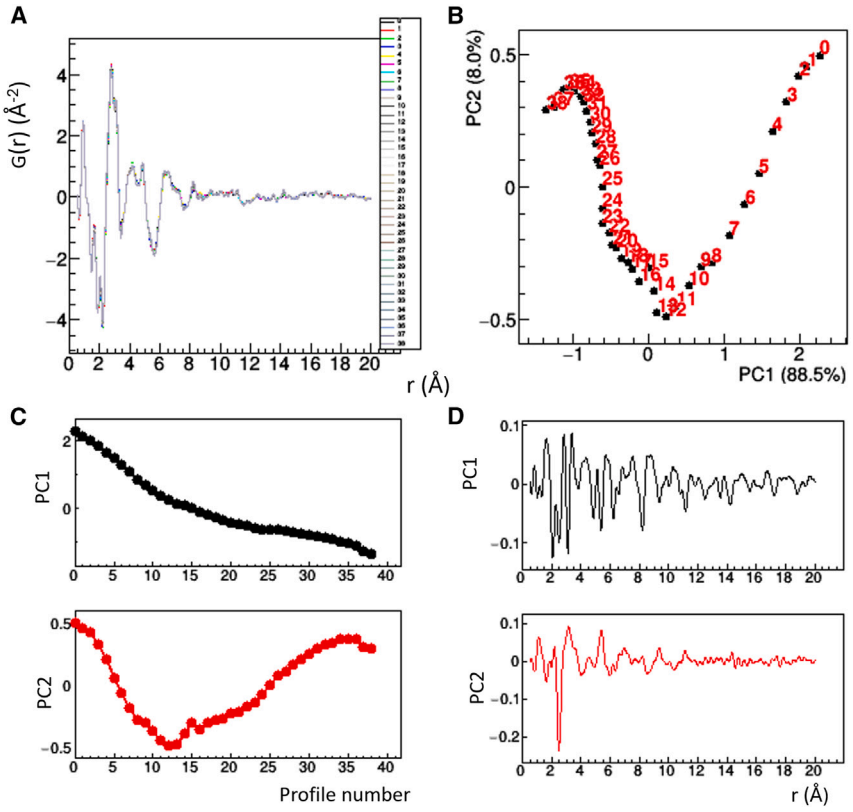

Figure 5. PCA comparison among PDF profiles without background subtraction obtained from *operando* measurements on sample NG3

(A) PDF profiles superposed.

(B) Score plot of the first two principal components. The percentage of data variance explained by each component is reported on its axis.

(C) Scores of the first 2 principal components.

(D) Loading plot of the first 2 principal components.

Electrochemical considerations

From a qualitative point of view, we were able to observe for each of the three samples the typical features relative to Ni electrochemistry. Peaks attributable to the $Ni^{2+} \leftrightarrow Ni^{3+\delta}$ transition are in fact visible in the 1.25–1.45 V potential range,[35] while the onset for the OER floats around 1.4 V. While we were able to acquire a single scan for NG1, we performed two consecutive electrochemical cycles for NG2 and NG3, as reported in Figure S12. The lower performances of sample NG3 with respect to NG1 and NG2 were attributed to a loss of catalyst mass during the conditioning cycles due to the production of O_2 gas, which in turn mechanically detaches some catalyst powder particles from the surface of the electrode. Interestingly, the same catalyst manifested an important change in the CV profile between the two subsequent cycles. The voltammetry plot in Figure S12A shows an important increase of both peaks related to the $Ni^{2+} \leftrightarrow Ni^{3+}$ transition, despite the reaching of a steady state during pre-conditioning of the electrocatalysts (scanned the cell between 1 and 1.6 V at a scan speed of 50 mV/s for 10 CV cycles).

Two-cycle data

For samples NG2 and NG3, we acquired the same series of PDF profiles for two consecutive cyclic voltammetries. Despite the quality of the second cycle, these data can be used to correlate the electrochemical system response (current) with that observed by XRD. Previous analysis on the first voltammetry cycle has shown that (1) the trend of PCA scores is similar in XRPD and PDF data, (2) PDF data provide the opportunity to interpret loading values in terms of changes in the local structure, and (3) background subtraction in the PDF could introduce differences among profiles that alter the score values. For these reasons, we opted to use PDF profiles without background subtraction to develop the analysis of the two-cycle data. PCA applied to these data from NG2 is shown in Figure 6. The 3D score plot, where the scores in the first three PCs are compared (Figure 6A), shows that the MED quadratic relationship (Equation 1) retains its validity between different score value planes. In the first voltammetry cycle, it holds between scores PC1 and PC3, while in the second cycle, it is valid between PC2 and PC3. Similarly, if the 3D score plot PC1-PC3-PC4 is considered, then the quadratic relationship holds between PC1 and PC4 in the first cycle and between PC3 and PC4 in the second cycle (data not shown). A rigorous application of the MED criterion, which requires a well-defined plane between two PCs where the quadratic relationship holds, is, therefore, not possible. Nevertheless, we observe that the trend of the PC3 and PC4 scores shown in Figure 6B correlates with that of the current shown in Figure 3B for the first voltammetry cycle. Conversely, the instability of the electrochemical cell encountered in the second cycle, probably due to the formation of air bubbles, introduces differences in the collected XRD data that disrupt the continuous trend of the PCA scores. Notably, both of the loading values associated with PC3 or PC4, which, according to the above arguments, can be considered as signals related to active atoms, exhibit the highest peak at 2.5 Å (Figure 6C).

Similar results are observed for the two-cycle data collected for NG3 (Figure 7). The pertinent MED plane in this case is formed by PC1 and PC2, at least in the first voltammetry cycle (Figure 7A). Here, a distinct correlation between the PC2 scores shown in Figure 7B and the trend of the current (Figure 3C) is evident in both cycles. Additionally, the trend of PC2 scores becomes constant toward the end of the second cycle, when the potential is halted while XRD measurements are still being collected. Consequently, PC2 can be linked to the system response attributed to active atoms, and its loading values (Figure 7C) still have a large peak at 2.5 Å, similar to the NG2 sample.

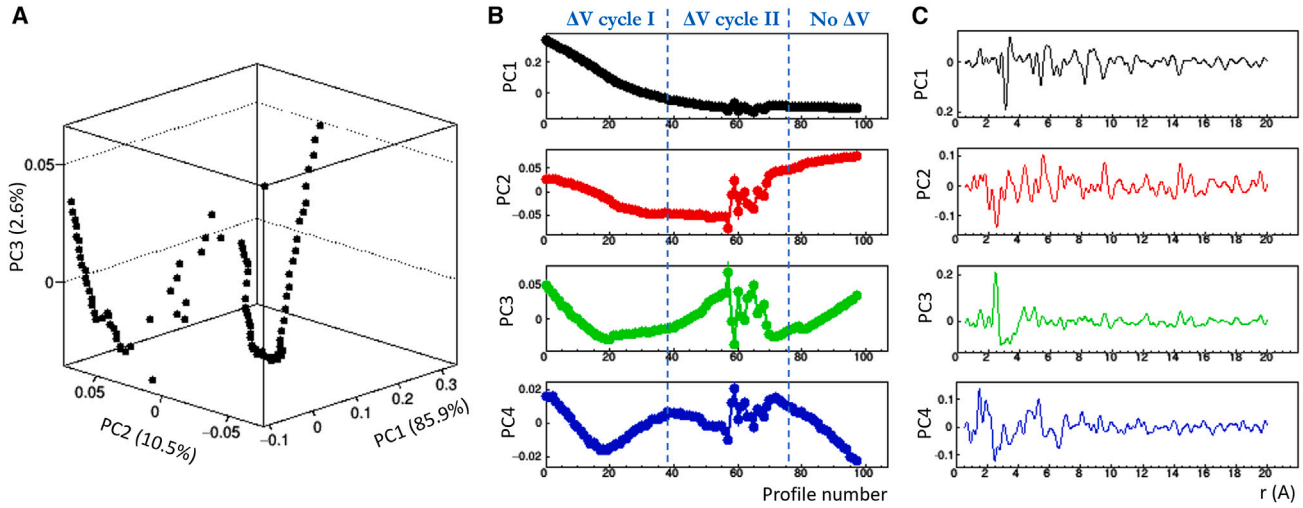

Figure 6. PCA comparison among PDF profiles without background subtraction obtained from *operando* measurements in two voltammetry cycles on NiGraf sample NG2

(A) Score plot of the first 3 principal components. The percentage of data variance explained by each component is reported on its axis.

(B) Scores of the first 4 principal components. Dashed lines denote the correspondence with the voltammetry cycles.

(C) Loadings of the first 4 principal components.

Structural interpretation of the system response to the electrochemical stimulus

The static PDF profiles of the three NiGraf samples considered in this study have been structurally interpreted: we identified the Ni and GO crystal phases present in the samples using COD numbers 9012316 (jamborite) and 9012236, respectively.[25] The PDF profiles calculated from these phases are depicted in Figure 8, alongside relevant views of the crystal structures. The same fitting parameters previously reported[25] were employed in the PDF calculations. Notably, the highest peaks in the PDF profile are located within 3.5 Å. Peaks at 1.5 and 2.5 Å originate from the GO phase, while those at 2.0 and 3.1 Å originate from the jamborite phase. Thus, they offer a unique fingerprint of the two crystal phases present in the samples. Based on this outcome, we can interpret the loading values obtained through model-free analysis of *operando* data in terms of the contribution from individual crystal phases and their possible changes.

We started with a study of the full stack of PDF data to determine the major changes in distances throughout the whole voltammetric cycle. Since PCA loadings contain differences between profiles, amplified by differential analysis and with a sign determined by the timing of their occurence during the *in situ* experiment, we have attempted a fit of the loading profiles determined related to the first two PCs (PC1 and PC2) with the PDF profiles calculated from the crystal phases present in the samples (jamborite and GO). Given the stronger correlation between electrochemical and XRPD responses observed for the NiGraf material NG3, we focused on PC1 and PC2 loadings obtained by PCA applied to the PDF profiles (without background subtraction) collected during the two voltammetry cycles on this sample. The scale factor, considered as free parameters in the fitting, was also allowed to be negative to account for intrinsic PCA sign ambiguity.

Fitting results, reported in Figure S13, show that most of the negative peaks of PC1 loadings are reproduced by the PDF profile calculated from jamborite (Figure S13A), while the GO phase gives a contribution to the huge negative peak at 2.5 Å, and that in PC2 loadings (Figures S13C and S13D), the two crystal structures appear with opposite signs, indicating opposite dynamic trends during the oxidation and reduction processes. The main contribution to the loading profiles comes from the interatomic distance of 2.5 Å (Figure S13D), which corresponds to the separation between nearby GO entities that develop along the c axis (Figure 8C). Conversely, the distances related to the GO hexagonal carbon ring along the b axis (Figure 8D) remain nearly unchanged. The role played by the Ni phase associated with oxidation-reduction cycles appears, therefore, to be minor. This could be attributed to the minimal effect of changes in the Ni oxidation state on varying the first-shell interatomic distances. A similar result is found for the NG2 sample when considering PC1 and PC3 loadings related to the two-cycle data. The predominant role of the GO phase, particularly the peak at 2.5 Å, in determining the PC3 loadings of NG2 (Figure 6C) and the PC2 loadings in NG3 (Figure S12C) indicates that the GO atoms with this interatomic distance behave as active atoms during the electrochemical process.

The loading values obtained from the PCA applied to single voltammetry cycles—as shown in Figure S5 for NG1, Figure 4 for NG2, and Figure 5 for NG3—are compared in Figure S14 by means of PCA. Only the significant PCs were considered, thus rejecting the components higher than 1 for NG1 and higher than 2 for NG2 and NG3. The shape of the loading profiles in Figure S14A and the arrangement of their representative points in Figure S14B indicate that NG2 and NG3 PC1 loadings are very similar and differ from the PC2 loadings of samples NG2 and NG3 as well as PC1 loadings of sample NG1. The main common feature of the first cluster of points (NG2 and NG3 PC1 loadings)

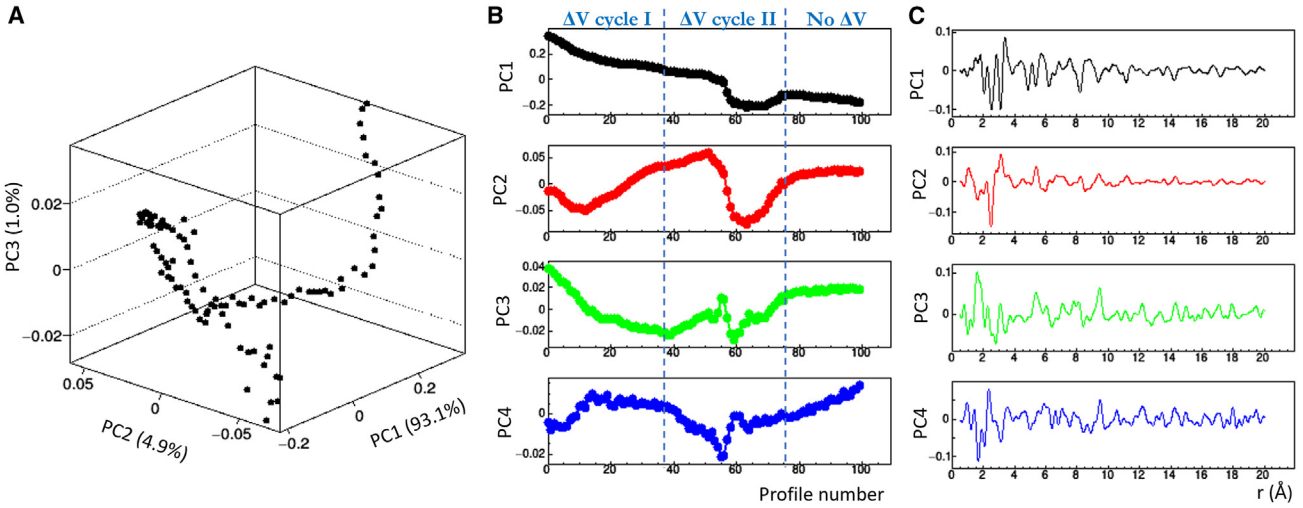

Figure 7. PCA comparison among PDF profiles without background subtraction obtained from *operando* measurements in two voltammetry cycles on sample NG3

(A) Score plot of the first 3 principal components. The percentage of data variance explained by each component is reported on its axis.

(B) Scores of the first 4 principal components. Dashed lines denote the correspondence with the voltammetry cycles.

(C) Loadings of the first 4 principal components.

is a significant (negative) PDF peak at 3.1 Å, which corresponds to the Ni–Ni distance in the jamborite phase (Figure 8B). On the other hand, the main feature in the second cluster of points (NG2 and NG3 PC2) is a substantial (negative) PDF peak at 2.5 Å, which is associated with the distance among C columns along the c axis in the GO phase (Figure 8C). The PC1 loadings of NG1, despite having a characteristic peak at 3.1 Å, are more akin to the PC2 points.

Potential-dependent principal-component analysis

To assess the influence of the electrochemical stimulus on the structure of the nanoparticles, we applied PCA on subsets of *operando* PDF profiles identified along the voltammetric scan. As a first step, this study was performed by considering both voltammetric scans of sample NG2 and NG3 and dividing the single scans in three subset regions, (1) an anodic ramp subset, (2) an anodic still subset, and (3) a cathodic ramp subset, as visible in Figure 9, where the PCA scores obtained within each subset of profiles are reported using a color scale. No significant results were obtained from the application of the potential-dependent PCA to the NG1 sample, as the limited changes occurring among PDF profiles made the within-interval PCA scores statistically irrelevant.

The most noteworthy peaks were identified at 2.0, 2.5, 3.1, 4.8, 5.3, 6.2, 8.2, and 9.3 Å and are highlighted with bars and letters in Figure 9. With reference to Figures 8 and S15, peaks denoted by the letter *c* were associated with Ni–Ni distances of the jamborite phase, peak *b* was associated with the GO phase, and *a* peaks have contributions from both the GO phase and Ni–O distances of the jamborite phase. The PCA scores obtained in each interval were corrected for sign ambiguity by considering the sign of the jamborite peaks at 5.3, 8.2, and 9.3 Å, all corresponding to distances between more distant Ni atoms. The results, plotted in Figure 9, where the color threshold changes between subsets, express a variation between background-subtracted integrated PDF series. This means that the bigger the signal at a certain *r* for a certain subset, the higher the variation from the precedent subset. The results are similar for the two samples and highlight anti-correlated variations between peak *b*, from GO, and *c* peaks from the jamborite Ni–Ni distances. Moreover, it can be noted that for the first CV cycle (segments 0, 1, and 2), NG2 does not show the *b* signal related to GO, as expected due to the low loading, and signal *c* is also present in the anodic part of the first voltammetric scan (segment 0).

On the contrary, for NG3, signal *b* is clearly visible at lower potentials (segment 0). The second voltammetric cycle, on the contrary, shows a similar response with respect to the PDF between the samples. For both NG2 and NG3, in the initial part of the anodic scan (segment 3), the peaks are in line with the ones present in the last segment of the first CV cycle (segment 2). Conversely, in the middle and terminal parts of the second scan (segments 4 and 5), a strong signal from GO (*b*) emerges from both samples, which was not present during the first CV, while all the other jamborite signals fade. A fine PDF sampling on the first voltammetric cycle of sample NG3 was also carried out. This time, the voltammetric cycle for the NiGraf sample with the highest GO signals due to its higher loading was divided into six different time/potential ranges, each one comprising 6 PDF measurements covering 400 s of the voltammetric scan and defining three potential ranges for the half scan: (1) from 1.06 to 1.40 V, (2) from 1.40 to 1.74 V, and (3) from 1.73 to 2.06 V. The first three ranges could thus be associated with the anodic (forward) scan and the last three with the backward (cathodic) scan. The rescaled values of the PCA scores calculated in each interval are shown in Figure 10.

Therein, peaks labeled as *a*, due to the Ni–O distances from the jamborite phase and C–C distances from the GO phase, do

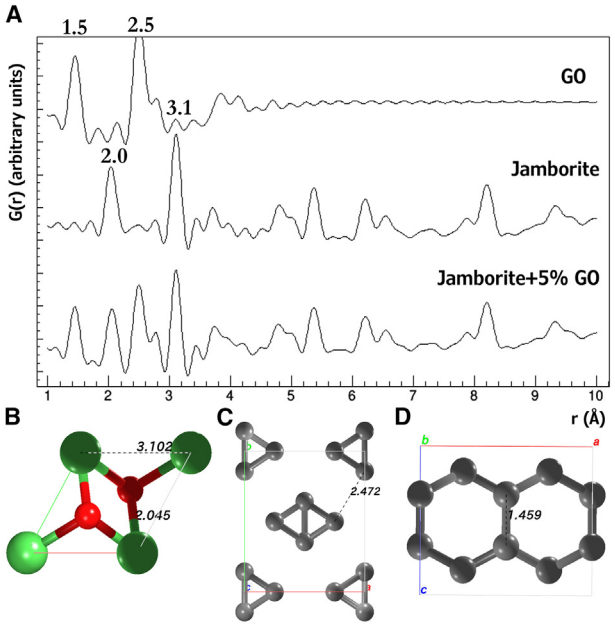

Figure 8. Structural interpretation of PDF profiles

(A) PDF profiles calculated from the crystal phases identified in sample NG3: Ni-phase COD 9012316 (jamborite) and GO-phase COD 9012236.

(B) View along the c axis of the structural fragment of the Ni phase, with Ni and O atoms colored in green and red, respectively.

(C) View along the c axis of the GO phase.

(D) View along the b axis of the GO phase. Relevant distances are indicated in Å in the crystal structures and on the corresponding PDF peaks.

not seem to change with the voltammetric scan, while peak *b* and *c* peaks change their intensity in the different potential ranges. It may be noted how changes in *c* peaks are always correlated, as they correspond to Ni–Ni distances, while they appear to be anti-correlated with changes in peak *b*, which corresponds to GO interchain distances. In the most anodic part of the scan (Figure 10, ranges 3, 4, and 5), one can notice an increase in the intensities of *c* peaks and a decrease of that of peak *b*. On the other hand, for ranges 1, 2, and 6 in the most cathodic regions, an increase in *b* is visible, along with a decrease in *c*. Moreover, a splitting in *b* is observed at the highest oxidative potentials (range 4).

DISCUSSION

In brief, the analysis of *operando* XRD data applied to the new Ni-Graf electrocatalyst[25] has validated PCA as an effective approach for extracting trends from data. Similar trends are obtained using XRPD or PDF profiles, suggesting that the Fourier transform does not obscure any details within the data. Consequently, the evolution of the system during the experiment can equivalently be studied in reciprocal or direct space. Notably, it has been demonstrated that the primary limiting factor for *operando* experiments with low signal-to-background ratios, such as those utilizing an electrochemical cell, is the loss of coherence between successive profiles. Hence, experimental conditions need to ensure that any variation between two successive measurements is exclusively caused by alterations in the sample itself. In our study, this requirement was not met under certain conditions. Specifically, this occurred when conducting *operando* measurements in the XRPD setup, where the detector was positioned 1.4 m away from the sample (Figure S4). Additionally, this condition was not fulfilled when subtracting the background from individual profiles through offline analysis, especially when the signal from active atoms was very faint, as for the NG1 sample (Figure S6).

While trends in data can be equivalently extracted by analyzing XRPD or PDF profiles, the ability to interpret such changes leans decisively toward the PDF. When XRPD profiles are collected in a PDF setup, meaning with high energy of the primary beam and the detector at only 243 mm downstream of the sample, they suffer from low angular resolution and are often dominated by background from diffuse scattering. Consequently, Bragg peaks strongly overlap and become difficult to identify. In these conditions, recognizing structural variations of crystalline phases becomes difficult. Conversely, PDF profiles, which encode information on the local structure, are better suited for interpreting structural changes caused by active atoms and distinguishing them from the contributions of bulk and "silent" atoms. Moreover, PDF profiles are highly valuable for discerning significant components in PCA, as they have specific features characterizing their envelope and power spectrum. Thus, loadings showing a stronger contribution from high frequencies, like those shown in Figures S5 and S6, can be deemed insignificant.

The interpretation of loadings obtained by applying PCA to PDF *operando* measurements in terms of structural features was facilitated by prior static measurements on the same NiGraf samples.[25] In previous measurements, the samples were characterized in terms of crystal phase identification and structural fitting. This prior characterization enabled us to interpret the loadings by leveraging the fact that the PDF profiles of the two crystal phases present in the samples have well-defined and separated characteristic peaks, located in the first 3.2 Å interatomic distances (Figure 8). Two pairs of peaks were assigned to jamborite and GO phases. This assignment guided our interpretation of the loading values obtained through the PCA.

The MED framework did not strictly apply for all samples due to the simultaneous contributions of two active atoms: one from the jamborite phase and the other from the GO phase. While the applied voltage induces a change in the oxidation state of the Ni atoms in jamborite, transitioning from Ni^{2+} to Ni^{3+}, it also triggers a structural alteration in both the metal and carbon phases, affecting the mutual distance among carbon chains stacked along the c axis, and the Ni–Ni distances. It could be hypothesized that the prolonged stress of the electrocatalyst in the range of gas evolution could play a role in the changes visible in the GO structural features (Figures 9 and 10, peak *b*). These changes, which are probably related to a loss in the stacking order of the graphene phase, are reversible within the first voltammetric cycle but became irreversible for the second one, especially for the NG3 sample. Moreover, the complexity of the system's response results in variability in the order of PCs holding the relevant MED information, which must be identified on a case-by-case basis. Analysis of the loadings shows that changes in the

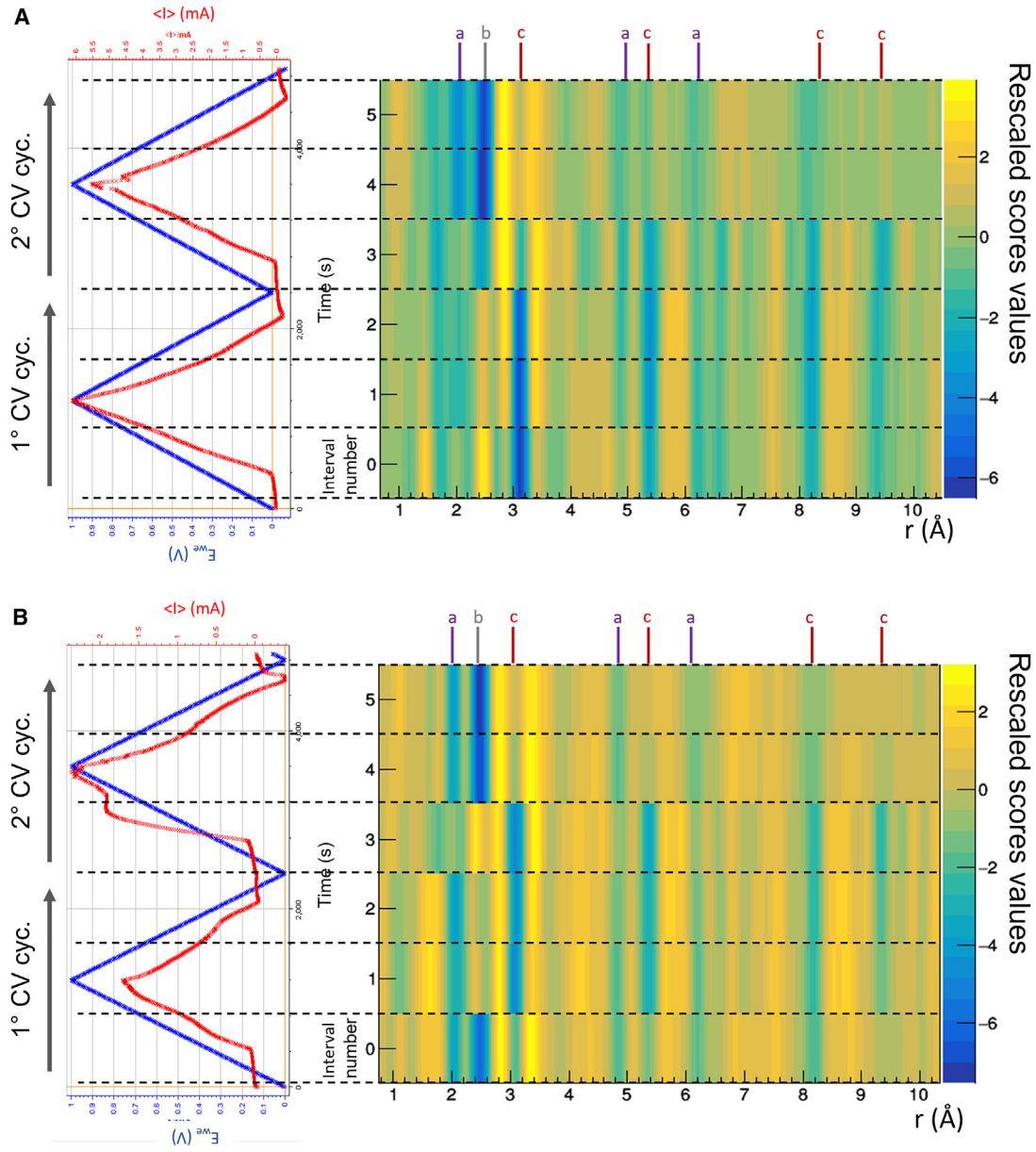

Figure 9. Results of the potential-dependent PCA

Scores of the potential-dependent PCA during both CV cycles for the NG2 (A) and NG3 (B) NiGraf samples. The left charts depict the potential (*E*) vs. time (in blue) and the current (*I*) vs. time (in red) during voltammetry. The two voltammetric cycles for each sample are divided in six intervals of PDF measurements, each interval comprising 12 PDF measurements. The color code for the rescaled score values is shown on the right vertical axis. *c* signals are relative to the 3.1, 5.3, 8.2, and 9.3 Å PDF Ni–Ni peaks of the jamborite phase, while the *b* signal at 2.5 Å is associated with the GO phase. Signals *a* at 2.0, 4.9, and 6.2 Å have contributions from both Ni–O jamborite peaks and the GO phase.

two phases are in counterphase, as indicated by their corresponding PDF peaks having opposite signs in the loadings (Figures 6 and 7).

These conclusions are reinforced by the comparative analysis of the loadings derived from processing the PDF profiles collected during a single voltammetry cycle for the three samples (Figure S14). Within the framework of the MED theory, this analysis can be interpreted as follows: the PC1 loadings from NG2 and NG3 are connected to the mixed-atom contribution (active + silent atoms), and they are dominated by a characteristic PDF peak at 3.1 Å of the jamborite phase. On the contrary, the PC2 loadings from the same samples are linked to the active atom contribution, predominately featuring the PDF peak at 2.5 Å of the GO phase.

It is noteworthy that the interatomic distances of the two crystal phases involved in the structural changes are not those within the first coordination shell. The shortest distances, such as Ni–O (PDF peak at 2.0 Å) for jamborite and C–C (PDF peak at 1.5 Å) for

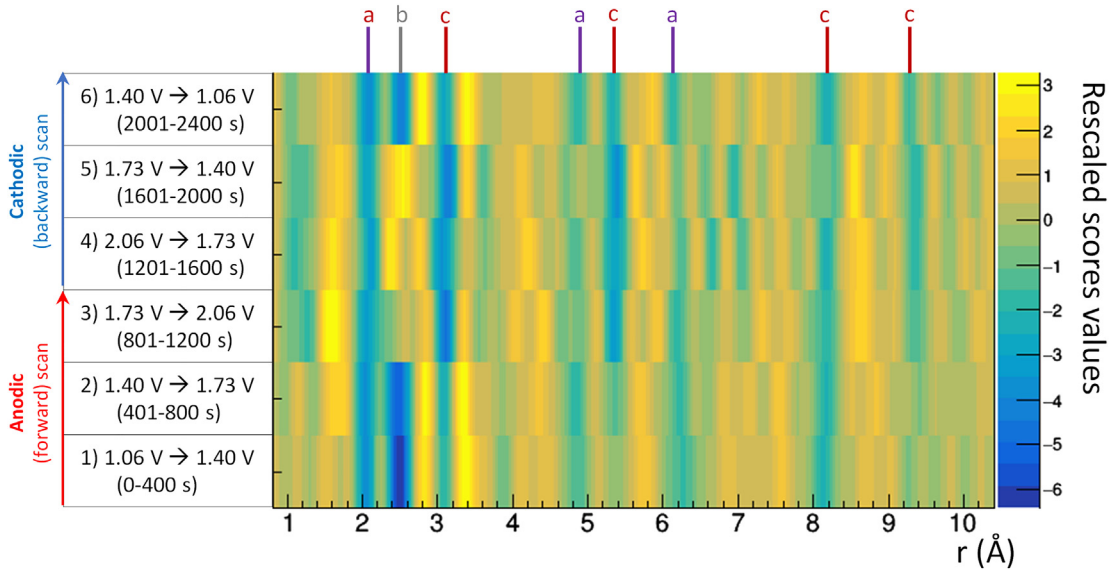

Figure 10. Scores of the potential-dependent PCA during the first CV cycle of the NG3 NiGraf sample

The voltage values and time during the CV scan corresponding to the six intervals of PDF measurements are shown on the left vertical axis. Each interval comprises 6 PDF measurements. The color code for the rescaled score values is shown on the right vertical axis. *c* signals are relative to the 3.1, 5.3, 8.2, and 9.3 Å PDF Ni–Ni peaks of the jamborite phase, while the *b* signal at 2.5 Å is associated with the GO phase. Signals *a* at 2.0, 0.4.9, and 6.2 Å have contributions from both Ni–O jamborite peaks and the GO phase.

GO, are not featured prominently in the loading profiles attributed to active atoms. These distances are strongly constrained by a chemical bond, which remains relatively unperturbed by the *in situ* electrochemical stimulus. Instead, the most significant contribution to the MED signal arises from the PDF peak at 2.5 Å of the GO phase, corresponding to an interatomic distance associated with crystal packing. This observation suggests that the electrochemical stimulus primarily affects weaker intermolecular interactions rather than the stronger intramolecular ones, resulting in structural changes that are evident prominently in the PDF profiles. The method of the potential-dependent PCA applied to PDF profiles confirms this trend and shows another interesting characteristic of this novel molecularly doped metal: the peaks from the GO phase and the Ni–Ni jamborite phase intensify in counterphase with respect to each other. This is evident from both Figures 9 and 10. Particularly, as shown in Figure 10, at lower potentials (below OER potentials), the peak related to GO entity distances (2.5 Å) remains clearly visible and fades in intensity at higher oxidative potentials, returning to its original state during the backward voltammetric scan. This outcome suggests a loss in order in the GO phase at the potentials at which the OER occurs, which is reversibly re-acquired when the potentials are brought back to the initial values. On the other hand, the signals associated with different Ni–Ni distances in the jamborite phase (*c* peaks in Figures 9 and 10), which are nearly absent at lower potentials, strengthen in the ranges at which higher oxidative potentials are applied. All this happens while signal *a*, representative of the Ni–O distance and more distant C–C atoms in GO, remains unaffected by the applied potential stimulus.

Weakening of the Ni–Ni signal from the PCA scores in the second scan of NiGraf samples NG2 and NG3, displayed in Figure 9, was investigated by studying the evolution of the PDF profiles during the two-cycle *in situ* experiments (Figure S15). It can be noted that peaks become narrower and sharper as the experiment progresses, following a continuous trend *not* correlated with voltage variations, which could be related to the monotonic trend obtained for the PC1 scores in most of the PCAs performed on these metal-organic alloy (MORAL) samples. Moreover, Figure S15 shows that this evolution reaches a plateau for the PDF profiles collected during the decrease of potential in the second scan. These PDF profiles seem to vary less than in the other regions, and this is the reason why the differential analysis performed by the voltage-dependent PCA affords weaker signals in intervals 4 and 5 of Figure 9. This quenching of the structural signal from X-rays is accompanied by a stronger measured current. Hence, this effect is likely due to a stabilization of the NiGraf electrocatalyst, which emerges from the initial transient phase characterized by important structural changes. The stabilization phase is probably related to the activation of the catalyst itself, which, apart from the initial conditioning CV cycles, has to incur oxidative stress in order to prepare its NiOOH surface for electrochemical oxidation.[36]

Operando PDF experiments using electrochemical cells pose challenges due to significant background contributions that vary throughout the experiment. This difficulty is particularly pronounced when the catalytic material is deposited in the cell as an "ink" on a conductive support. Under such conditions, surface electrochemical effects may dominate, distinct from the bulk material that is not actively participating in the reaction.

Our study provides a protocol for optimizing such experiments, which includes both experimental setup and data analysis. From the experimental point of view, we demonstrated that by simply making a hole in the conductive carbon support, it is possible to improve the signal-to-noise ratio and eliminate

structured background contributions with a minor loss in electrochemical signal. A careful alignment of the cell, which can be monitored by collecting XRPD data by changing the position of the empty cell, makes it possible to center the X-ray beam on the aperture. In addition, we found that the typical PDF setup, with the detector very close to the sample, minimizes the fluctuations of the diffraction signal due to the scattering of air or sampling different regions of the detector. Accordingly, we were able to extract regular trends in data by processing the PDF measurements, from which the response of the system can be monitored. Conversely, no discernible trend in the data could be identified through analysis of XRPD measurements, necessitating placement of the detector at a considerable distance from the sample.

From the computational point of view, we used PCA for the fast monitoring of data during the execution of the experiment and to highlight differences in data. With this tool, we identified a consistent trend by analyzing data through PCA in reciprocal space (XRPD profiles) or in direct space (PDF profiles calculated from the previous XRPD profiles), thus proving that calculations of total scattering and Fourier transform do not introduce artifacts in the PDF profiles. PCA results were interpreted in terms of active and silent atoms in light of the MED approach. In this context, PCA scores (calculated from XRPD or PDF profiles) are used to recognize the MED quadratic relationship and identify the candidate PCs holding the signal from active atoms. In addition, the OCCR method is applied to NG3 data to introduce constraints into PCA, i.e., to find new directions for the PCs that describe the data according to the MED hypotheses. Then, PCA loadings calculated from PDF profiles are used to check the significance of the PCs, by comparing them with the features of an ideal PDF profile, and infer changes in the local structure that are responsible for the trend in data captured by the given PC.

In the case of two voltammetric cycles, we show that the system response can be captured by different PCs in the two cycles. Moreover, the application of MED analysis to our MORAL samples is not straightforward because (1) for the NG1 NiGraf sample, the structural changes of the unique phase present (jamborite) are limited, so only one PC is significant, and (2) for NG2 and NG3 NiGraf materials, two types of active atoms, arising from the two crystal phases (GO and jamborite), are present, and their changes are captured by the same PC.

A very interesting result from the catalysis viewpoint was obtained when studying the correlation between the electrochemical and structural responses of the molecularly doped metal. A potential-dependent PCA was introduced to obtain dynamic information about the onset of structural changes during the voltammetric cycles. For the NiGraf sample with the highest loading of GO, the variation in score values from the potential-dependent PCA of the *in situ* PDF profiles reveals a distinct and reversible trend during the initial voltammetric cycle. Specifically, it is the signal from the GO that intensifies at higher oxidative potentials. On the other hand, at lower potentials, the signal related to the jamborite Ni–Ni bond grows in intensity at the beginning and the end of the first cycle, and it is heavily reduced after the second cycle. This could indicate a stabilization of the active phase of the catalyst (the activation of the catalyst itself) that follows a transient regime dominated by a crosstalk between the jamborite and GO phases. This unique synergy phenomenon arises from the 3D entrapment of GO within the jamborite nanocrystallites characteristic of MORALs,[37] distinguishing it from previously developed decorated GO/Ni electrocatalysts.[20,38] Therefore, it serves as a promising foundation for future studies on the reactivity of NiOx/GO systems.

EXPERIMENTAL PROCEDURES

Sample preparation

The NiGraf samples analyzed in this study, NG1, NG2, and NG3, have GO loads of 0.2, 1.0, and 5.0 wt %, respectively. They have been synthesized as previously reported.[25] The NiOx particles have a dimension between 50 and 100 nm. GO in aqueous solution (8 mg/mL, product code NG01GO0501) was purchased from Nanografi Nano Technology (Çankaya/Ankara, Türkiye). The solution consists of 1–5 μm large GO microparticles varying in thickness between 0.4 and 1.1 nm.[39]

Electrochemical experiment

The electrochemical cell has been specifically designed to carry out *operando* PDF measurements. The sample is mounted on the cell with this procedure: first, an ink is prepared by mixing 2 mg of the powdered sample with 500 μL water, 500 μL ethanol, and a few drops of Nafion ionomer. Then, the ink is sonicated for 20 min, and 200 μL is drop casted on the pin-holed exposed part of the CP previously inserted in the cell. It was allowed to dry, and finally the cell was closed with the other Kapton window. For the electrochemical measurements, a Pt wire was used as the CE, while an Ag/AgCl/KCl Sat. electrode was used as the RE. All the potentials are expressed vs. RHE. *In situ* and *operando* measurements were performed using an electrolytic solution of 1 M KOH (Sigma-Aldrich) in Milli-Q water, while a Biologic VSP-300 potentiostat was used to control the experiments. The single voltammetries of each electrocatalyst were coupled with the voltammetry of the pin-holed CP substrate, acquired using the same experimental setup, in order to highlight the small influence of the substrate on the overall OER electrochemistry. Prior to the PDF voltammetric cycle, 10 CV scans in the range 1–1.6 V vs. RHE using a scan speed of 50 mV/s were performed to condition the WE.

PDF measurements

PDF profiles were collected at the 28ID-2 beamline of the National Synchrotron Light Source (NSLS-II) of the Brookhaven National Laboratory, USA, with an X-ray energy of 68.36 keV (0.1814 Å) and a 0.5 × 0.5 mm beam size. Measurements were performed in transmission mode and at room temperature. The beamline is equipped with two PerkinElmer XRD 1621 digital imaging detectors, each consisting of a flat CsI-coated scintillator panel whose active area is formed by 2,048 × 2,048 pixels with size 200 × 200 μm. They were mounted orthogonal to the beam path, at 243 and 1,411 mm downstream of the sample, according to a setup optimized for PDF and XRPD measurements, respectively. Static measurements were carried by filling Lindemann capillaries with powder samples. An empty capillary was measured for background estimation, and cerium oxide was measured as a standard material to calibrate the wavelength and the detector position. *Operando* measurements were carried out by mounting the electrochemical cell perpendicular to the beam, as shown in Figure 2A. Each measurement took 1 min (45 s acquisition time + 15 s dead time). Three subsequent background measurements were taken in the same conditions and then averaged. The potential to the electrodes was supplied on site by a Biologic BCS-810 potentiostat positioned outside the experimental hutch. The cell without a sample but filled with the electrolytic solution was used for measuring the background estimation. Measurements were carried out at different cell positions, and for each position, three images were acquired and averaged to increase the signal over background ratio.

XRD data analysis

Diffraction images were azimuthally integrated and converted into intensity XRPD profiles vs. momentum transfer $q = 4\pi\sin\vartheta/\lambda$ using the DIOPTAS program.[40] PDF profiles were calculated from the q profiles with the program PDFGetX3.[41] The parameters for PDF calculation (background subtraction, scale factor, minimum and maximum values of q, degree of data-correction

polynomial) were optimized on individual PDF profiles to avoid large termination effects and preserve the signal-to-noise ratio. The q_{max} value used for PDF generation is reported in Table S1. The collected patterns and PDF profiles were compared by PCA using the RootProf program.[42,43] PCA loadings obtained from PDF data were fitted with structural models using the program PDFgui.[44]

A potential-dependent variant of PCA was implemented in the program RootProf according to the following protocol: several PCA runs were performed sequentially on subsets of the measured profiles, identified by considering the trend of the potential applied in the voltammetric cycles. The score values obtained by PCA applied on each subset of measurements were corrected for sign ambiguity; rescaled by a standard normal variate transformation, i.e., subtracted by their mean and divided by their standard deviation; and plotted as a function of the interval number. The protocol adopted for the potential-dependent PCA is similar that developed for the space-dependent PCA applied in Caliandro et al.[45]

MED theory

MED is a technique that allows selective detection of active atoms by the analysis of *operando* XRD measurements in systems where they are clearly separated from the bulk silent atoms and belong to a single-crystal phase.[46] According to MED predictions, the signal from active atoms can be extracted from data due to its specific behavior in the time domain. In fact, it is expected to vary with time at double the frequency of the stimulus variation. If data are processed by PCA, then the signal from active atoms is expected to uniquely contribute to the loadings of a specific PC, which needs to be identified out of the many components in which data are decomposed by looking at the score values. The MED signal concerns two PCs (*PCx* and *PCy*) linked by a quadratic relationship among their scores value, i.e.,

$$Scores_{PCy} = Scores_{PCx} * Scores_{PCx}. \quad \text{(Equation 1)}$$

Once the components that follow Equation 1, even approximately, are identified, the signal from active atoms is expected to uniquely contribute to the loadings of the component *PCy*. In case of active atoms belonging to a single-crystal phase, the loading values of *PCy* are expected to have a definite sign and represent the X-ray profile from active atoms only.[26]

RESOURCE AVAILABILITY

Lead contact

The lead contact is Mario Pagliaro (mario.pagliaro@cnr.it).

Materials availability

This study did not generate new unique reagents.

Data and code availability

All data and code reported in this paper will be shared by the lead contact upon request.

ACKNOWLEDGMENTS

This research was funded by the European Union – NextGeneration EU through the Ministero dell'ambiente e della sicurezza energetica, POR H2 AdP MMES/ENEA, with the involvement of CNR and RSE, PNRR - Mission 2, Component 2, Investment 3.5 "Ricerca e sviluppo sull'idrogeno," CUP: B93C22000630006. We thank Rocco Lassandro, CNR-IC, for support in carrying out the synchrotron measurements at BNL. We thank Carlo Bartoli, CNR-ICCOM, for the electrochemical cell production and design. Access to the National Synchrotron Light Source (Brookhaven National Laboratory, NY, USA) was supported by the US Department of Energy, Office of Science, Office of Basic Energy Sciences, under contract no. DE-SC0012704 (NSLS-II proposal no. 312211). E.B. acknowledges the Made in Italy - Circular and Sustainable (MICS) Extended Partnership funded by the European Union – NextGeneration EU (Piano Nazionale di Ripresa e Resilienza [PNRR] - Missione 4, Componente 2, Investimento 1.3 – D.D. 1551.11-10-2022, PE00000004) for financial support.

AUTHOR CONTRIBUTIONS

Conceptualization, R.C., E.B., A.L., R.C., M.P., and C.G.; resources, E.B., R.C., A.L., V.M., R.C., C.G., and M.P.; methodology, R.C., E.B., and V.M.; validation, R.C., C.G., A.L., and V.M.; investigation, R.C., E.B., M.V.P., and R.C.; data curation, R.C., E.B., M.V.P., and V.M.; formal analysis, E.B., R.C., C.G., and V.M.; visualization, E.B., R.C., V.M., and M.V.P.; writing – original draft, E.B. and R.C.; writing – review & editing, M.P., L.A., C.G., E.B., and R.C.; supervision, C.G., L.A., and M.P.; project administration, R.C., L.A., C.G., M.P., and E.B.; funding acquisition, R.C., C.G., M.P., and L.A.

DECLARATION OF INTERESTS

The authors declare no competing interests.

SUPPLEMENTAL INFORMATION

Supplemental information can be found online at https://doi.org/10.1016/j.xcrp.2024.102341.

Received: July 20, 2024
Revised: October 18, 2024
Accepted: November 21, 2024
Published: December 18, 2024

REFERENCES

1. Roldán Cuenya, B., and Bañares, M.A. (2024). Introduction: *operando* and *in situ* studies in catalysis and electrocatalysis. Chem. Rev. *124*, 8011–8013. https://doi.org/10.1021/acs.chemrev.4c00184.
2. Zhu, Y., Wang, J., Chu, H., Chu, Y.-C., and Chen, H.M. (2020). *In situ*/*operando* studies for designing next-generation electrocatalysts. ACS Energy Lett. *5*, 1281–1291. https://doi.org/10.1021/acsenergylett.0c00305.
3. Neumann, I., and Rasche, B. (2023). *In situ* diffraction in electrochemistry – A practical introduction for experiments beyond batteries. Curr. Opin. Electrochem. *39*, 101288. https://doi.org/10.1016/j.coelec.2023.101288.
4. Chapman, K.W. (2016). Emerging *operando* and x-ray pair distribution function methods for energy materials development. MRS Bull. *41*, 231–240. https://doi.org/10.1557/mrs.2016.26.
5. Borkiewicz, O.J., Shyam, B., Wiaderek, K.M., Kurtz, C., Chupas, P.J., and Chapman, K.W. (2012). The AMPIX electrochemical cell: a versatile apparatus for *in situ* X-ray scattering and spectroscopic measurements. J. Appl. Crystallogr. *45*, 1261–1269. https://doi.org/10.1107/S0021889812042720.
6. Young, M.J., Bedford, N.M., Jiang, N., Lin, D., and Dai, L. (2017). *In situ* electrochemical high-energy X-ray diffraction using a capillary working electrode cell geometry. J. Synchrotron Radiat. *24*, 787–795. https://doi.org/10.1107/S1600577517006282.
7. Diaz-Lopez, M., Cutts, G.L., Allan, P.K., Keeble, D.S., Ross, A., Pralong, V., Spiekermann, G., and Chater, P.A. (2020). Fast *operando* X-ray pair distribution function using the DRIX electrochemical cell. J. Synchrotron Radiat. *27*, 1190–1199. https://doi.org/10.1107/S160057752000747X.
8. Bulavchenko, O.A., and Vinokurov, Z.S. (2023). *In situ* X-ray diffraction as a basic tool to study oxide and metal oxide catalysts. Catalysts *13*, 1421. https://doi.org/10.3390/catal13111421.
9. Ciriminna, R., and Pagliaro, M. (2023). Enhanced nickel catalysts for producing electrolytic hydrogen. RSC Sustain. *1*, 1386–1393. https://doi.org/10.1039/d3su00177f.
10. Huo, L., Jin, C., Jiang, K., Bao, Q., Hu, Z., and Chu, J. (2022). Applications of nickel-based electrocatalysts for hydrogen evolution reaction. Adv. Energ. Sus. Res. *3*, 2100189. https://doi.org/10.1002/aesr.202100189.
11. Machado, S.A.S., and Avaca, L.A. (1994). The hydrogen evolution reaction on nickel surfaces stabilized by H-absorption. Electrochim. Acta *39*, 1385–1391. https://doi.org/10.1016/0013-4686(94)E0003-I.

12. Juodkazis, K., Juodkazytė, J., Vilkauskaitė, R., and Jasulaitienė, V. (2008). Nickel surface anodic oxidation and electrocatalysis of oxygen evolution. J. Solid State Electrochem. *12*, 1469–1479. https://doi.org/10.1007/s10008-007-0484-0.

13. Chen, Y., Rui, K., Zhu, J., Dou, S.X., and Sun, W. (2019). Recent progress on nickel-based oxide/(oxy)hydroxide electrocatalysts for the oxygen evolution reaction. Chem. Eur J. *25*, 703–713. https://doi.org/10.1002/chem.201802068.

14. Miller, H.A., Bouzek, K., Hnat, J., Loos, S., Bernäcker, C.I., Weißgärber, T., Röntzsch, L., and Meier-Haack, J. (2020). Green hydrogen from anion exchange membrane water electrolysis: a review of recent developments in critical materials and operating conditions. Sustain. Energy Fuels *4*, 2114–2133. https://doi.org/10.1039/C9SE01240K.

15. Santoro, C., Lavacchi, A., Mustarelli, P., Di Noto, V., Elbaz, L., Dekel, D.R., and Jaouen, F. (2022). What is next in anion-exchange membrane water electrolyzers? Bottlenecks, benefits, and future. ChemSusChem *15*, e202200027. https://doi.org/10.1002/cssc.202200027.

16. Hassan, Q., Sameen, A.Z., Salman, H.M., and Jaszczur, M. (2023). Large-scale green hydrogen production via alkaline water electrolysis using solar and wind energy. Int. J. Hydrogen Energy *48*, 34299–34315. https://doi.org/10.1016/j.ijhydene.2023.05.126.

17. Radinger, H., Connor, P., Tengeler, S., Stark, R.W., Jaegermann, W., and Kaiser, B. (2021). Importance of nickel oxide lattice defects for efficient oxygen evolution reaction. Chem. Mater. *33*, 8259–8266. https://doi.org/10.1021/acs.chemmater.1c02406.

18. Wang, H., Xue, J., Liu, C., Chen, Z., Li, C., Li, X., Zheng, T., Jiang, Q., and Xia, C. (2023). CO_2 electrolysis toward acetate: A review. Curr. Opin. Electrochem. *39*, 101253. https://doi.org/10.1016/j.coelec.2023.101253.

19. Zhao, Y., You, J., Wang, L., Bao, W., and Yao, R. (2021). Recent advances in Ni_3S_2-based electrocatalysts for oxygen evolution reaction. Int. J. Hydrogen Energy *46*, 39146–39182. https://doi.org/10.1016/j.ijhydene.2021.09.137.

20. Han, X., Suo, N., Chen, C., Lin, Z., Dou, Z., He, X., and Cui, L. (2019). Graphene oxide guiding the constructing of nickel-iron layered double hydroxides arrays as a desirable bifunctional electrocatalyst for HER and OER. Int. J. Hydrogen Energy *44*, 29876–29888. https://doi.org/10.1016/j.ijhydene.2019.09.116.

21. Zhou, A., Bai, J., Hong, W., and Bai, H. (2022). Electrochemically reduced graphene oxide: Preparation, composites, and applications. Carbon *191*, 301–332. https://doi.org/10.1016/j.carbon.2022.01.056.

22. Dreyer, D.R., Todd, A.D., and Bielawski, C.W. (2014). Harnessing the chemistry of graphene oxide. Chem. Soc. Rev. *43*, 5288–5301. https://doi.org/10.1039/C4CS00060A.

23. Fruehwald, H.M., Moghaddam, R.B., Melino, P.D., Ebralidze, I.I., Zenkina, O.V., and Easton, E.B. (2021). Ni on graphene oxide: a highly active and stable alkaline oxygen evolution catalyst. Catal. Sci. Technol. *11*, 4026–4033. https://doi.org/10.1039/D1CY00297J.

24. González-Ingelmo, M., García, M.L., Oropeza, F.E., Álvarez, P., Blanco, C., Santamaría, R., and Rocha, V.G. (2023). Ultra-high dispersion of Ni-based OER catalysts on graphene 3D networks enhances the in situ Fe^{3+} catalytic activation. J. Mater. Chem. A *11*, 24248–24260. https://doi.org/10.1039/D3TA04481E.

25. Pagliaro, M., Pagliaro, M.V., Caliandro, R., Giannini, C., Ciriminna, R., and Lavacchi, A. (2024). NiGraf: a new nickel-based molecularly doped metal for enhanced water electrolysis. Mater. Adv. *5*, 2759–2766. https://doi.org/10.1039/d3ma00700f.

26. Chernyshov, D., Van Beek, W., Emerich, H., Milanesio, M., Urakawa, A., Viterbo, D., Palin, L., and Caliandro, R. (2011). Kinematic diffraction on a structure with periodically varying scattering function. Acta Crystallogr. A *67*, 327–335. https://doi.org/10.1107/S0108767311010695.

27. Caliandro, R., Chernyshov, D., Emerich, H., Milanesio, M., Palin, L., Urakawa, A., van Beek, W., and Viterbo, D. (2012). Patterson selectivity by modulation-enhanced diffraction. J. Appl. Crystallogr. *45*, 458–470. https://doi.org/10.1107/S0021889812011569.

28. Berretti, E., Pagliaro, M.V., Giaccherini, A., Montegrossi, G., Di Benedetto, F., Lepore, G.O., D'Acapito, F., Vizza, F., and Lavacchi, A. (2022). Experimental evidence of palladium dissolution in anodes for alkaline direct ethanol and formate fuel cells. Electrochim. Acta *418*, 140351. https://doi.org/10.1016/j.electacta.2022.140351.

29. Berretti, E., Giaccherini, A., Montegrossi, G., D'Acapito, F., Di Benedetto, F., Zafferoni, C., Puri, A., Lepore, G.O., Miller, H., Giurlani, W., et al. (2019). *In-situ* quantification of nanoparticles oxidation: a fixed energy X-ray absorption approach. Catalysts *9*, 659. https://doi.org/10.3390/catal9080659.

30. Montegrossi, G., Giaccherini, A., Berretti, E., Benedetto, F.D., Innocenti, M., d'Acapito, F., and Lavacchi, A. (2017). Computational speciation models: a tool for the interpretation of spectroelectrochemistry for catalytic layers under operative conditions. J. Electrochem. Soc. *164*, E3690–E3695. https://doi.org/10.1149/2.0711711jes.

31. Neder, R.B., and Proffen, T. (2020). Exact and fast calculation of the X-ray pair distribution function. J. Appl. Crystallogr. *53*, 710–721. https://doi.org/10.1107/S1600576720004616.

32. Chapman, K.W., Lapidus, S.H., and Chupas, P.J. (2015). Applications of principal component analysis to pair distribution function data. J. Appl. Crystallogr. *48*, 1619–1626. https://doi.org/10.1107/S1600576715016532.

33. Caliandro, R., Guccione, P., Nico, G., Tutuncu, G., and Hanson, J.C. (2015). Tailored multivariate analysis for modulated enhanced diffraction. J. Appl. Crystallogr. *48*, 1679–1691. https://doi.org/10.1107/S1600576715017070.

34. Guccione, P., Lopresti, M., Milanesio, M., and Caliandro, R. (2020). Multivariate analysis applications in x-ray diffraction. Crystals *11*, 12. https://doi.org/10.3390/cryst11010012.

35. Diaz-Morales, O., Ferrus-Suspedra, D., and Koper, M.T.M. (2016). The importance of nickel oxyhydroxide deprotonation on its activity towards electrochemical water oxidation. Chem. Sci. *7*, 2639–2645. https://doi.org/10.1039/c5sc04486c.

36. Klaus, S., Cai, Y., Louie, M.W., Trotochaud, L., and Bell, A.T. (2015). Effects of Fe electrolyte Impurities on $Ni(OH)_2$/NiOOH structure and oxygen evolution activity. J. Phys. Chem. C *119*, 7243–7254. https://doi.org/10.1021/acs.jpcc.5b00105.

37. Avnir, D. (2018). Recent progress in the study of molecularly doped metals. Adv. Mater. *30*, 1706804. https://doi.org/10.1002/adma.20170680430.

38. Munde, A.V., Mulik, B.B., Chavan, P.P., and Sathe, B.R. (2020). Enhanced electrocatalytic activity towards urea oxidation on Ni nanoparticle decorated graphene oxide nanocomposite. Electrochim. Acta *349*, 136386. https://doi.org/10.1016/j.electacta.2020.136386.

39. Nanografi Nano Technology, Graphene Oxide Water Dispersion 8 mg/mL, https://nanografi.com/graphene/graphene-oxide-dispersion-8-mg-ml-in-h2o/ (accessed July 11, 2024)

40. Prescher, C., and Prakapenka, V.B. (2015). DIOPTAS: a program for reduction of two-dimensional X-ray diffraction data and data exploration. High Pres. Res. *35*, 223–230. https://doi.org/10.1080/08957959.2015.1059835.

41. Juhás, P., Davis, T., Farrow, C.L., and Billinge, S.J.L. (2013). PDFgetX3: a rapid and highly automatable program for processing powder diffraction data into total scattering pair distribution functions. J. Appl. Crystallogr. *46*, 560–566. https://doi.org/10.1107/S0021889813005190.

42. Caliandro, R., and Belviso, D.B. (2014). RootProf: software for multivariate analysis of unidimensional profiles. J. Appl. Crystallogr. *47*, 1087–1096. https://doi.org/10.1107/S1600576714005895.

43. Mazzone, A., Lopresti, M., Belviso, B.D., and Caliandro, R. (2023). New features of the RootProf program for model-free analysis of unidimensional profiles. J. Appl. Crystallogr. *56*, 1841–1854. https://doi.org/10.1107/S1600576723008348.

44. Farrow, C.L., Juhás, P., Liu, J.W., Bryndin, D., Božin, E.S., Bloch, J., Proffen, T., and Billinge, S.J.L. (2007). PDFfit2 and PDFgui: computer programs for studying nanostructure in crystals. J. Phys. Condens. Matter *19*, 335219. https://doi.org/10.1088/0953-8984/19/33/335219.

45. Caliandro, R., Altamura, D., Belviso, B.D., Rizzo, A., Masi, S., and Giannini, C. (2019). Investigating temperature-induced structural changes of lead halide perovskites by *in situ* X-ray powder diffraction. J. Appl. Crystallogr. *52*, 1104–1118. https://doi.org/10.1107/S160057671901166X.

46. Palin, L., Caliandro, R., Viterbo, D., and Milanesio, M. (2015). Chemical selectivity in structure determination by the time dependent analysis of *in situ* XRPD data: a clear view of Xe thermal behavior inside a MFI zeolite. Phys. Chem. Chem. Phys. *17*, 17480–17493. https://doi.org/10.1039/C5CP02522B.